



Article

Film Thickness and Friction of Textured Surfaces in Hydrodynamic Inclined and Parallel Gaps—An Experimental Study

Petr Šperka ^{1,*}, Jan Knotek ¹, Milan Omasta ¹, Ivan Křupka ¹, Pavel Polach ² and Martin Hartl ¹

¹ Faculty of Mechanical Engineering, Brno University of Technology, Technická 2, 616 69 Brno, Czech Republic; milan.omasta@vut.cz (M.O.)

² Faculty of Applied Sciences, University of West Bohemia in Pilsen, Technická 8, 301 00 Pilsen, Czech Republic

* Correspondence: petr.sperka@vut.cz

Abstract

This paper presents an experimental study on the influence of surface texturing on friction and film thickness in the hydrodynamic lubrication regime. Using a pin-on-disk tribometer equipped with light-induced fluorescence microscopy, simultaneous measurements were conducted on smooth and textured samples under parallel and inclined surface conditions. The circular faces of the pins were partially or fully covered by circular laser-machined textures consisting of dimples with depths of 5 or 10 μm , diameters of 50 or 100 μm , and coverage density of 20%. The results demonstrate that while texturing significantly reduces friction and increases film thickness in parallel gaps, with partial inlet coverage being the most effective, its impact is minimal in inclined wedge gaps. The study further reveals that the global geometric wedge dominates over texture effects in inclined contacts and that in-texture cavitation, prevalent in parallel conditions, is suppressed by surface inclination. Three distinct contributions of the textures were discussed: a global hydrodynamic effect, a local hydrodynamic effect, and the influence of surface non-flatness (waviness). The findings suggest that texturing is primarily beneficial for acting as a pseudo-wedge or as surface roughness in contacts where a physical wedge is absent.

Keywords: hydrodynamic lubrication; plain bearing; surface texturing; friction; parallel surfaces; film thickness measurement

1. Introduction

Friction and wear of sliding surfaces are significant factors influencing the performance and lifespan of mechanical components. Nowadays, Laser Surface Texturing (LST) and other microfabrication techniques enable the precise control of texture geometry, density, and distribution. The application of these textures has been investigated across a spectrum of mechanical components, including thrust bearings, journal bearings, mechanical seals, cylinder liners, and piston rings. The primary objective in these applications is to enhance hydrodynamic lubrication performance, characterized by increased load-carrying capacity, reduced friction coefficients, and expanded fluid film regimes. By manipulating the fluid flow at the micro-scale, texturing aims to bridge the gap between boundary lubrication and full fluid film lubrication, pushing the Stribeck curve transition to lower speeds and higher loads. Recent developments were the theme of numerous review papers, with some of the most relevant to this work being [1–3].



Received: 10 December 2025

Revised: 26 December 2025

Accepted: 4 January 2026

Published: 6 January 2026

Copyright: © 2026 by the authors.

Licensee MDPI, Basel, Switzerland.

This article is an open access article

distributed under the terms and

conditions of the [Creative Commons](https://creativecommons.org/licenses/by/4.0/)

[Attribution \(CC BY\)](https://creativecommons.org/licenses/by/4.0/) license.

The classical Reynolds equation, which serves as the foundation of hydrodynamic lubrication theory, assumes laminar flow between smooth surfaces, where the lubricant is entrained into a wedge gap with pressure-driven flow (known as Poiseuille flow) acting against it, driving the outflow from the contact. Many studies have demonstrated the potential of surface texturing to enhance tribological performance, with a prevailing consensus that partial texturing is superior to full texturing for generating substantial hydrodynamic load-carrying capacity [4–6]. Surface texturing introduces discontinuities that challenge these assumptions, necessitating consideration of several potential contributions. Brizmer et al. [4] identified a pseudo-wedge effect in partial texturing analogous to a stepped slider, whereas full texturing primarily relies on individual local cavitation effects and is less effective for load support. Cupillard et al. [7] further clarified that the pressure build-up mechanism functions through energy transfer in the inlet, comparable to a convergence ratio modification, but warned that excessive texture depth induces turbulence effects, which diminish the pressure gradient. Manser et al. [8] demonstrated that variable-depth (wedge-bottom) profiles provide superior load lift compared to flat-bottom shapes due to the micro-wedge action, and Hsu et al. [9] emphasized the importance of feature orientation, finding elliptical shapes perpendicular to the sliding direction to be most effective for friction reduction across lubrication regimes. Codrignani et al. [6] established a linear scaling law between the optimal dimple depth and the operating gap height.

The role of cavitation within textures remains a subject of intense debate. While often modeled theoretically using mass-conserving algorithms, experimental validation of the interaction between texture-induced cavitation and macroscopic bearing inclination is limited. Bai et al. [10] observed cavitation formation in textures and found that cavitation occurs at the entrance to the texture and gradually expands in the direction of lubricant flow. In several studies [11,12], experiments on cavitation behavior in textures under different experimental conditions were presented. Understanding how the pressure perturbations of partial texturing interact with the physical convergence of a slider bearing is critical for optimizing components that operate under varying inclination angles, such as piston rings [13,14] and tilting-pad bearings [15].

Light-induced fluorescence (LIF) has emerged as a versatile optical technique [16–20] that overcomes several limitations of interferometry, particularly the requirement for reflective surface coatings and a limited unambiguous film thickness range. The method utilizes a fluorescent dye dissolved in the lubricant, which, when excited by a light source such as a laser, narrowband LED, or mercury lamp, absorbs radiation and re-emits it at a longer wavelength, a phenomenon known as the Stokes shift. According to the Beer–Lambert law, the intensity of this emitted fluorescence is proportional to the thickness of the liquid film, provided the film is thin, and the dye concentration is sufficiently low. This technique enables the simultaneous measurement of film thickness and the observation of phenomena such as cavitation and oil distribution over larger areas than those typically accessible by other optical methods.

The interferometry technique was successfully applied to hydrodynamic contacts [21–25]. While LIF provides high spatial resolution and facilitates three-dimensional surface reconstruction, its accuracy can be influenced by optical distortions [26] caused by steep interface slopes and system heterogeneity, which may necessitate advanced calibration procedures, such as pixel-dependent methods [27], to mitigate nonlinear errors. Other methods, such as electrical capacitance and eddy current sensors, are also utilized [28]; however, eddy current probes can be invasive if positioned within the contact or suffer from accuracy loss due to component deformation if mounted externally. Additionally, ultrasonic reflection methods [29] offer a non-invasive alternative for measuring films through various

engineering materials, although they require sophisticated signal processing to resolve thin films.

The aim of this research is to elucidate the formation of the lubrication film in sliding contact with textured surfaces under conditions of parallel and inclined surfaces in the hydrodynamic lubrication regime. It applies the light-induced fluorescence (LIF) method within a modified universal tribometer to conduct simultaneous measurements of film thickness and friction force. By utilizing direct film thickness data to evaluate the actual wedge inclination in real-time, this methodology ensures a more precise interpretation of the interaction between texture-generated pseudo-wedge effects, in-texture cavitation, and global geometric convergence. Consequently, this work represents one of the first experimental investigations to systematically analyze these simultaneous parameters in nominally parallel gaps, offering new insights into how surface texturing enhances performance when a physical wedge is absent.

2. Materials and Methods

The goal of the experiment was to simultaneously measure the thickness of the lubricating film and the coefficient of friction in the sliding hydrodynamic contact with controlled wedge gap geometry. The contact was formed between a glass disk of 150 mm diameter and the flat face of a 6 mm diameter cylindrical pin. A commercially available universal tribometer, RTEC MFT-5000 (Rtec Instruments, San Jose, CA, USA), configured to pin-on-disk, was modified and complemented by a light-induced fluorescence microscope. The load cells were replaced by more rigid models (100 N range for normal force and 50 N range for friction direction, HBK S2M, and accuracy class 0.02), especially against bending and twisting. The pin was fixed in a custom tip-tilt mechanism with sensitivity of inclination control 0.001° (i.e., slope change of $0.1 \mu\text{m}$ on a pin diameter of 6 mm). Its configuration is shown in Figure 1. A stationary steel pin is fixed in the tip-tilt mechanism and connected to load cells through a spring in the normal direction and a rotary joint in the friction direction, with its axis aligned in a plane of the frictional interface. The pin is located on the top of the glass disk and rotated by a servo drive from the original tribometer. The microscope is placed on an XY linear table, while the light path from the objective is reflected to the contact interface from the bottom side via a 90° optical prism. The optical prism is placed on another tip-tilt adjustment mechanism, and a diaphragm is placed above the prism. A linear servo actuator with feedback control applies the load.

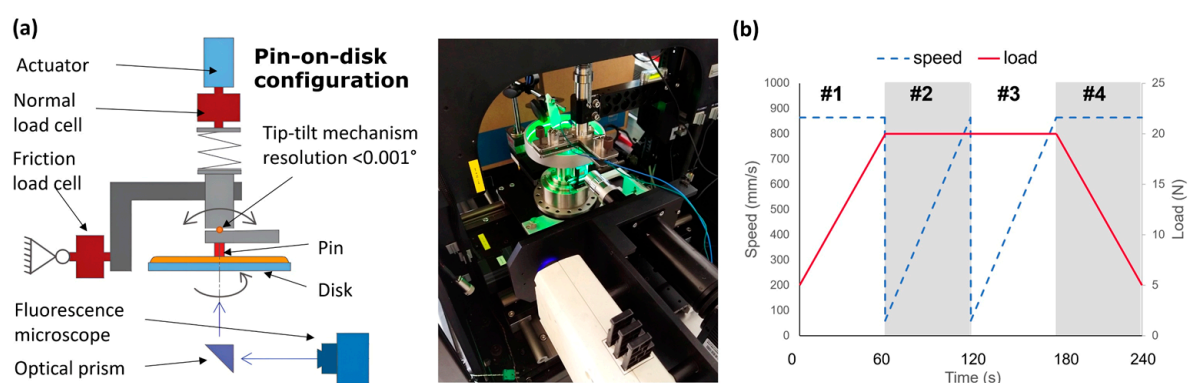


Figure 1. (a) Scheme and photograph of the modified universal tribometer with a light-induced fluorescence microscope; (b) scheme of test sequence.

The light-induced fluorescence technique is based on the photoexcitation of fluorescence-sensitive materials and the measurement of emitted light intensity, which is proportional to film thickness. There is a wavelength shift between excitation and emission light, which

is separated by a set of filters and a dichroic mirror inside the microscope. Within the area of thin films, there is a linear proportionality between emission light intensity and gap thickness. The linear relationship was checked to hold up to 50 μm thickness for the current configuration. The current microscope setup uses a 415 nm narrowband LED light source, a 19001 AT—Aqua longpass filterset (Chroma Technology Corp., Bellows Falls, VT, USA), a 16-bit monochrome CMOS camera (Tucsen, Fuzhou, China, FL20BW, Sony IMX183 sensor, 20 MPixel, $2.4 \times 2.4 \mu\text{m}$ pixel size), and a $2\times$ magnification long working-distance microscope objective. The microscope field of view is $6.55 \times 4.4 \text{ mm}$. Images were captured by Micromanager software and processed in MatlabR2023b.

The pin is made of 100Cr6 bearing steel, and the glass disk is from BK7 optical glass without any coating. Due to a chamfer on the steel pin edge, the effective flat part of the pin face has a diameter of $5.25 \pm 0.1 \text{ mm}$. The surface was lapped to a flatness of $0.1 \mu\text{m}$ or better, evaluated on 90% diameter of the effective face area. The top of the bearing surface has an RMS roughness of $\leq 70 \text{ nm}$. Six textured samples were prepared by laser machining, and one non-textured sample for reference. Laser textures were prepared using a picosecond laser ablation process on Perla[®]100 (Hilase, Dolní Břežany, Czech Republic). Circular textures were considered, with a designed surface coverage density of 20%. Textured samples were classified by diameter (100 μm , 50 μm), depth (10 μm , 5 μm), full/half area coverage, and, additionally, the pattern of texture distribution (hexagonal, herringbone). Parameters of samples are listed in Table 1, Table 2, and the scheme of dimples distribution is shown in Figure 2. The RMS surface roughness Sq was calculated according to the ISO 25178-2 standard [30], including the texture features. The input data were processed for term removal by fitting a sphere to obtain the optimum curvature R_s . No additional filtration was applied prior to the Sq evaluation. The RMS value of surface waviness Wq is defined analogously to Sq , except that it was calculated from long-pass filtered data with a cutoff wavelength of 0.2 mm. This filter was applied after term removal and masking out texture features, so that only the waviness of the land area is included. Finally, the height of the mean plane shift H_s was determined within the textured area by establishing a zero-mean plane; the shift was identified in the height distribution histogram as the distance from the zero value to the center of the bins corresponding to the land area. A detailed height map with a profile of the fabricated texture dimples is shown in Figure 3.

Table 1. List of pin samples with parameters and texture configuration.

Sample	Textures Coverage	Diameter d (μm)	Depth h (μm)	Pattern
D1	$\frac{1}{2}$ (Figure 2b)	100	10	Herringbone (Figure 2d)
D2	1 (Figure 2a)	100	10	Herringbone (Figure 2d)
D3	$\frac{1}{2}$ (Figure 2b)	100	5	Hexagonal (Figure 2e)
D4	$\frac{1}{2}$ (Figure 2b)	50	5	Herringbone (Figure 2d)
D5	$\frac{1}{2}$	100	10	Hexagonal (Figure 2e)
D6	$\frac{1}{4}$	100	10	Herringbone (Figure 2d)
C1	-	-	-	-

Table 2. Parameters of sample surface geometry.

Sample	C1	D1	D2	D3	D4	D5	D6
RMS surface roughness in place of texture Sq (μm)	0.07	3.797	3.886	1.94	1.43	3.15	3.54
Height shift of the mean surface plane H_s (μm)	~ 0	1.68	1.82	0.879	0.658	1.38	1.57
Surface flatness, radius of curvature R_s (m)	50.5	159.4	31.2	127.1	45.2	56.7	35.6
RMS value of surface waviness height Wq (μm)	0.045	0.026	0.063	0.055	0.144	0.068	0.087

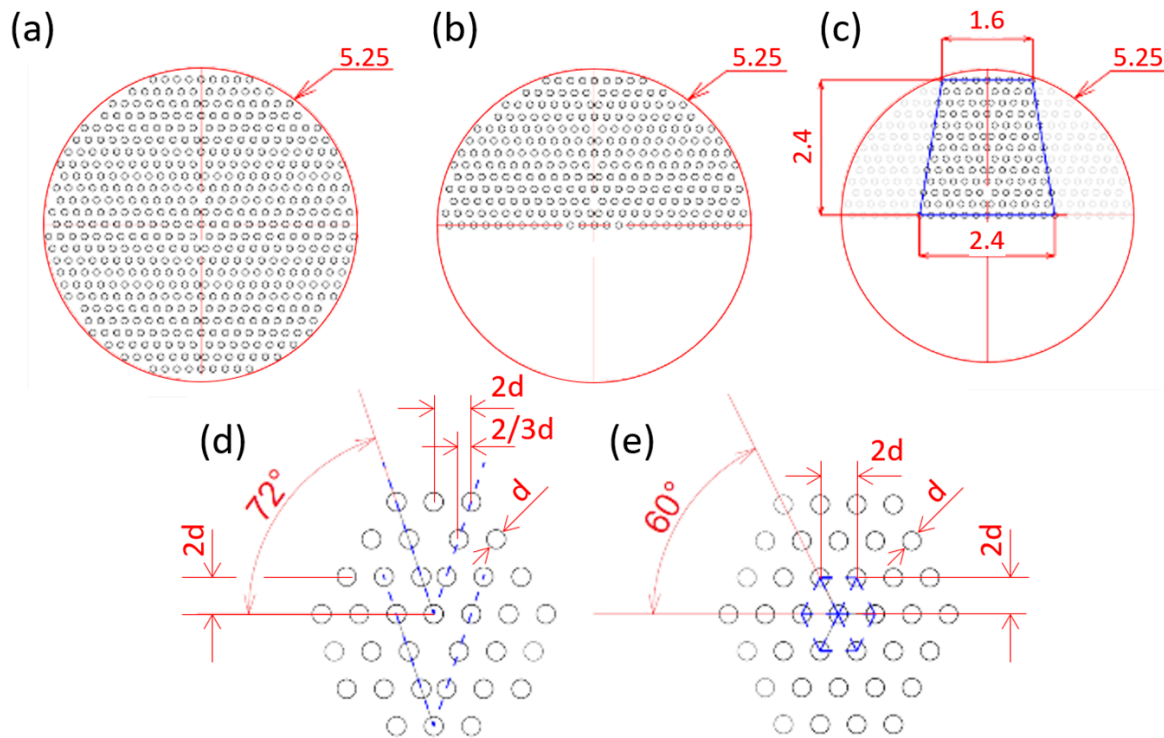


Figure 2. Scheme of three considered texture coverages: (a) full, (b) half at contact inlet, and (c) quarter at contact inlet. Patterns of texture distribution: (d) herringbone and (e) hexagonal.

A standard chemical substance Trioctyl Trimellitate (TOTM, CAS: 3319-31-1), purchased from Sigma Aldrich (Merck, Darmstadt, Germany) with 99% purity, was used as the lubricant. It is a well-defined hydrocarbon substance with medium viscosity. Dynamic viscosity is 225.2 mPa·s at 24 °C. The low-shear viscosity dependence of dynamic viscosity on temperature is described by the Vogel relation $\eta = 1.926 \times 10^{-5} \cdot \exp [1316/(t + 116.5)]$, where η is in Pa·s and temperature t in °C. Experiments were conducted at the ambient temperature of 24.5 ± 1 °C. The TOTM was mixed with Coumarin 6 fluorescence dye in a concentration of 0.02 wt%. The dye was dissolved in ethanol, mixed with a lubricant, and the solvent was then evaporated under magnetic stirring. The solution was stable for several months without evident separation or dye crystallization.

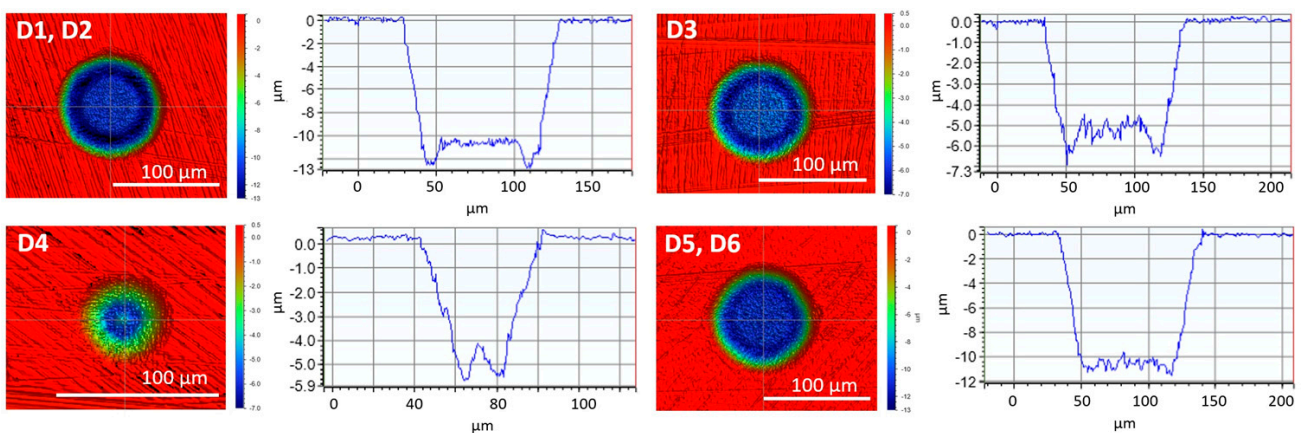


Figure 3. Shape and profiles of textures produced on the samples.

The test sequence contained four blocks (#1–#4), whereby in #1, the load was increased from 5 to 20 N under the constant speed of 865 mm/s, followed by two repetitions (#2 and #3) of speed increases from 50 to 865 mm/s at the constant load of 20 N, while the final #4 block saw a load decrease from 20 N to 5 N (see Figure 1b). Each block took 60 s, forces and actual speeds were sampled at 100 Hz, and film thickness was acquired once every second. The sequence was selected to show consistency and stability of the test configuration. Each experiment was repeated three times. Experimental conditions are listed in Table 3.

Table 3. List of operational conditions.

Property	Value
Sliding speed, u	50–865 mm/s
Load, F	5–20 N
Pin area, S	21.6 mm ² (Ø 5.25 mm)
Wedge slope, δ	0, 3, 12 μ m
Temperature, t	24.5 \pm 1 $^{\circ}$ C

2.1. Fluorescence Method Calibration

There are several important steps to achieve reliable and accurate measurement by the light-induced fluorescence method:

- Flat-field normalization—to ensure the response of the microscope and optical system is equal in the whole field of view.
- Intensity-film thickness calibration—to precisely and accurately convert intensity levels to film thickness.
- Parasitic signal suppression—to decrease false signals being interpreted as signals of the physical lubricant layer.

Flat-field normalization is based on capturing a reference configuration of the gap with constant thickness filled by the lubricant (see Figure 4a). A precise shim of 20 μ m thickness separates the measurement BK7 glass disk and another optical glass window pressed by load through a light-absorbing homogeneous material. To improve the accuracy of the flat-field reference frame, an average of 5 frames or more was used, where individual frames were taken at a variable rotation of the steel shim. A built-in, so-called on-the-fly pre-processor function was used in Micro-Manager 1.4.23 software to instantly apply corrections during camera acquisition. Typically, the homogeneity of the image after correction was 2–3% within an 80% area of the microscope field-of-view, i.e., the area important for measurement.

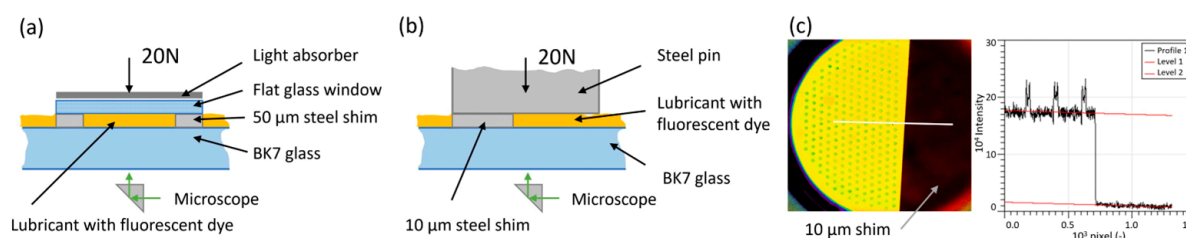


Figure 4. (a) Configuration for flat-field normalization; (b) configuration for film thickness calibration; (c) evaluation of step change due to shim thickness.

The calibration of fluorescence intensity to film thickness was obtained by pressing the 10 μ m thick steel shim between the BK7 glass disk, and a pin was used in the experiment (Figure 4b). It is important that the pin has the same reflectivity as that used in the experiment due to an additional effect of fluorescence dye excitation of the reflected beam.

The step change of intensity in the calibration frame was evaluated at five places, and the average value was taken as the conversion value for the given shim thickness (see Figure 4c). The standard deviation of the values in the set of profiles was typically 2%. The linear proportionality between the fluorescence signal and the gap was assumed. Note that with this procedure, it is incorrect to evaluate the thickness inside textures due to the difference in local reflectivity. The signal inside the dimples could even be lower than the signal at the bearing surface, despite the depth of a dimple extending the thickness of the local physical gap. The absolute accuracy of the calibration was checked according to the configuration of the wedge gap and measured by counting fringes of monochromatic interference. Accuracy was found to be better than 5%.

Especially under low film thickness conditions, an appropriate suppression of parasitic light sources, or at least their stabilization, is extremely important. The parasitic signal of light can be mistakenly interpreted as film thickness. The tribometer was covered by a black light-absorbing textile. Even in this configuration, there is always some background signal of a gap with zero thickness. Several reference frames with contact under static conditions were taken to obtain the background signal at the beginning and after each experiment. The background intensity is subtracted from each frame before conversion to film thickness.

In principle, the emission of fluorescence signal is in all directions; thus, next to the light directly collected by the microscope objective, there is a large amount of light emitted in directions that can be reflected and dispersed indirectly. In specific cases, it could provide a significant parasitic signal. One of the critical situations is under conditions of thin films and a large amount of lubricant present at the edge of the pin. Often, the thickness effectively excited in the inlet can be up to 20–100 times larger than that in the central zone. Practically, it exhibits an artificial intensity halo around the edge of the contact, with the pin appearing to have much worse flatness than the actual state. To suppress this major parasitic source, a diaphragm was placed above the optical prism just below the glass disk to limit the observation area to the contact zone. Moreover, the film thickness evaluation was performed in the central zone of the contact (at a maximum of 70–80% diameter).

The fluorescent dye can undergo photodegradation by excitation light, known as photobleaching. To decrease this effect, a pulsed LED excitation was used just within the camera integration time (typically 50–100 μ s). The photobleaching impact of the lubricant sample was checked in static conditions of the thickness calibration configuration, where a very minimal decrease in signal (less than 0.5%) was found within 4 min of the complete test period. Continuous illumination is often necessary for setting up the reference flat-field and the thickness calibration configurations. In these cases, the duration of fluorescent dye exposure to excitation was minimized as much as possible.

2.2. Film Thickness Evaluation

The main ideas of the measurement evaluation were to obtain a single value of central (or minimum) film thickness, and to obtain the film thickness representative of the bearing area of the surface left of textures. Three series of five points were manually picked on the measured frames, the same sets for the complete test sequence. At each point, an average of a near rectangular area several pixels wide and high was taken. At every set of five points, the best fit of a line was determined. From the line and knowledge of the pin beginning and the end, the central or minimum film thickness was calculated. The slope of the line was taken as the actual slope of the gap, individually evaluated for each frame. Film thickness data from three sets of points were compared, and their consistency was checked for potential outliers based on a threshold of the differences in the group of three values. The values free of outliers were averaged, and it was set as the single globally

representative value for the frame. A sample frame with a centerline profile, five points from a single point set, and a fitted line are shown in Figure 5.

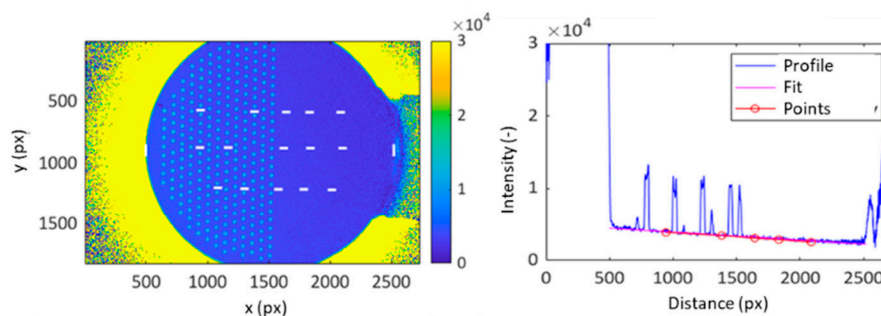


Figure 5. Sample fluorescence image with marked evaluation points (left part). Profile in the centerline, picked points, and line fit through the points (right).

2.3. Measurement Robustness

Figure 6a,b shows the result of a single experiment consisting of four blocks with the inclined smooth surface C1. On the x-axis, experimental conditions are plotted against a dimensionless hydrodynamic parameter, the same as that used by Raimondi and Boyd in [31], where η is the lubricant dynamic viscosity, B is the length of the slider, P represents the mean pressure, u is the sliding speed, and m is the relative slope of the surface defined as $(h_1 - h_m)/B$ with h_m and h_1 representing the film thickness at the exit and entrance to the gap, respectively. On the y-axis, the dimensionless central film thickness or dimensionless friction coefficient is plotted, where L is the width of the pin in the direction perpendicular to sliding. Data points from all four blocks create a single master curve with relatively small scattering. It demonstrates that the experimental setup consistently controls all key parameters of hydrodynamically lubricated contact.

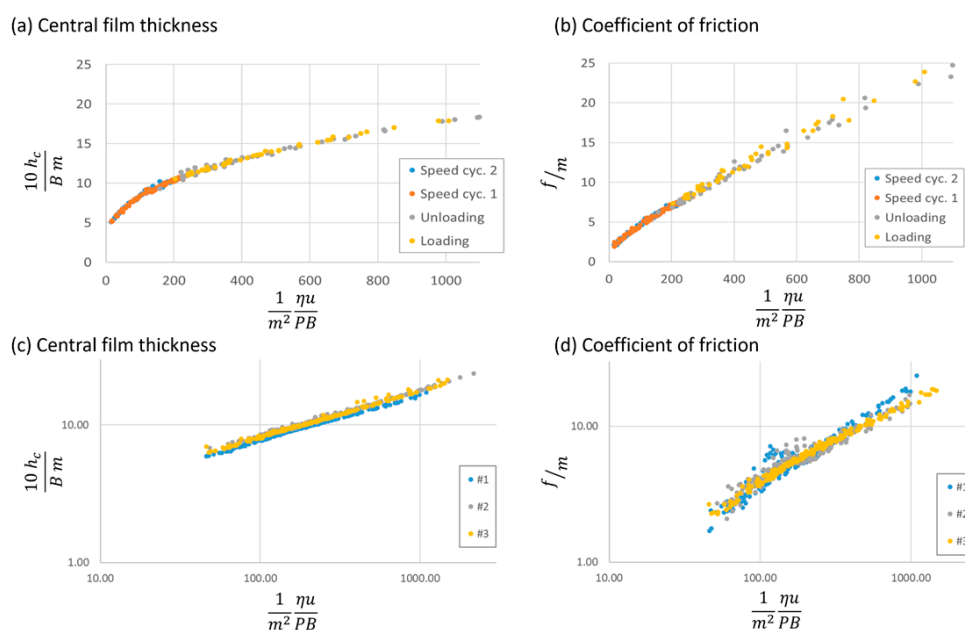


Figure 6. Plot of four blocks within a single measurement (a,b), and measurements repeated three times (c,d) against dimensionless hydrodynamic parameters on x- and y-axes.

Figure 6c,d presents three repetitions of the same operational conditions with the inclined untextured sample C1. The same dimensionless parameters are used on both axes. Data points from all four blocks with each repetition are now marked by the same color.

There is good overlap of measurement repetitions for central film thickness and friction, despite the fact that the frictional data show a slight divergence in high values of the x-axis. The central film thickness repetitions have relative variability of 3.9% and friction of 6.4% when differences are evaluated between power function best fits of individual measurement repetitions.

3. Results and Discussion

The results of the dimensionless minimum film thickness and the dimensionless coefficient of friction depending on the hydrodynamic dimensionless parameter for smooth and textured D6 samples and conditions of 0, 3, and 12 μm are shown in Figure 7. The definition of dimensionless parameters is according to Raimondi and Boyd from 1955 [31], where the actual inclination determined during evaluation for each frame (data point) is used for plotting. This strategy provides a narrower band of points compared to using a nominal constant value. In Figure 7, there is an overlap of the major part of the data points for inclined conditions (3 and 12 μm) into a narrow band, where it is difficult to determine the general difference in film thickness or friction between the smooth and textured samples. Additionally, two full lines represent the solution provided by Raimondi and Boyd [31] for L/B ratios of 1 and 0.5. The experimental points are plotted assuming a slider length B equal to the pin diameter of 5.25 mm and a slight, constant temperature rise of 2 $^{\circ}\text{C}$. For the given length B , the equivalent (equal area) slider width is 4.1 mm, resulting in an effective L/B ratio of 0.78. Although the contact conditions in the theoretical solution (rectangular slider) do not correspond to the experimental setup (circular slider), the trend is consistent for film thickness and moderately similar for friction. A small offset exists between the theoretical line and the virtual center of experimental point clouds. These deviations are likely linked to thermal effects, as the temperature rise increases at higher values of the hydrodynamic parameter.

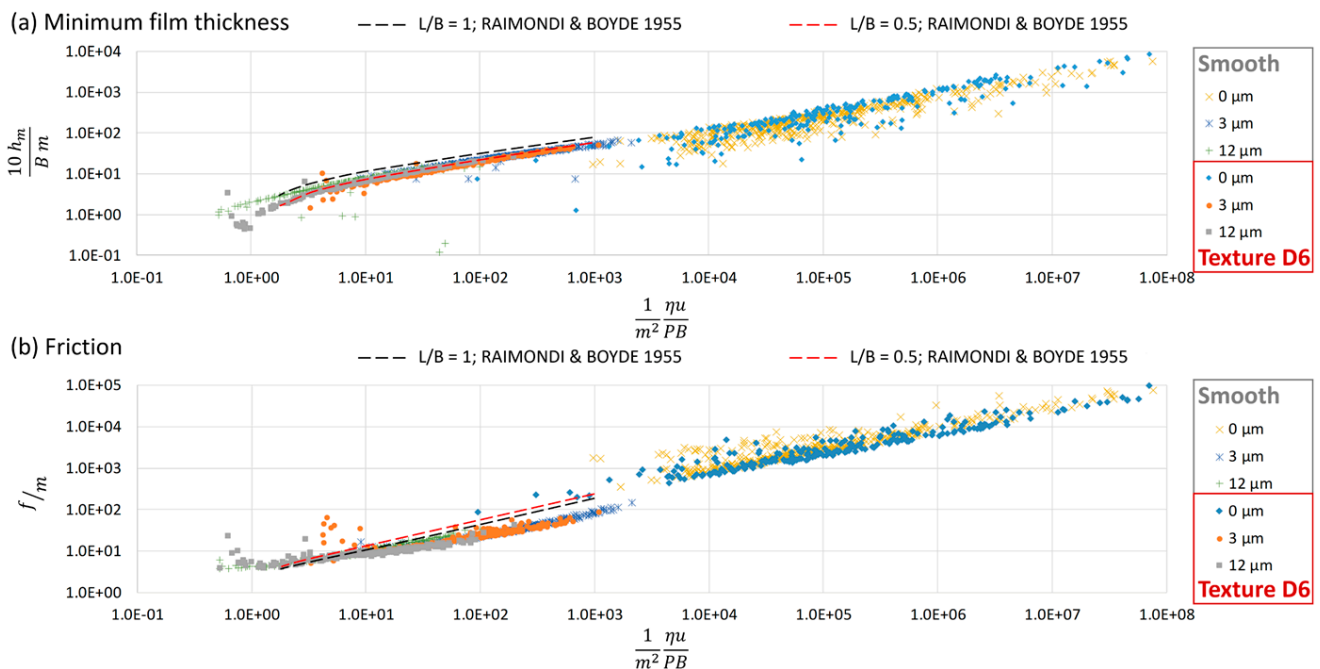


Figure 7. Smooth surface and texture D6 results plotted against dimensionless hydrodynamic parameters on x- and y-axes for (a) minimum film thickness and (b) friction [31].

Note that the results of ideal parallel surfaces cannot be plotted in this kind of plot due to the division by zero inclination in the definition of dimensionless parameters. For that reason, only the results of small positive inclinations are shown in the plot. Nevertheless, it

is interesting that points close to parallel contact (labelled as 0 μm) yield points that follow the trend of the inclined contacts relatively well, especially for the textured sample in terms of film thickness. In other cases, the slope of the trend line is similar, but a slight vertical offset is noticeable for the friction of both samples and the film thickness of the smooth sample. For parallel contact, the results show that the textured sample D6 provides a thicker film and lower friction. The reason for the offset can be due to either a measurement discrepancy or additional physical effects not included in the classical hydrodynamic theory, such as thermal distortion, thermal wedge phenomena, in-contact cavitation, or in-texture flow variation. The measurement discrepancy may be related to the effect of severe mathematical sensitivity to very small inclinations, where even small random or systematic errors can significantly impact plot accuracy. It is difficult to decide which of these causes the offset.

Since it is inappropriate to plot the parallel contact results and difficult to evaluate the percentage difference between the reference (smooth sample) and the textured sample from a dimensionless plot (Figure 7), an alternative approach was chosen. The goal was to determine the average values of friction and film thickness for each condition within a fixed range of operating conditions. The process is illustrated in Figure 8a for a cycle with variable speed (labeled the Speed cycle) and parallel surfaces, and in Figure 8b for a cycle with variable load (labeled the Force cycle) and inclined surfaces. To ensure the statistical representativeness of the measured data points and the same conditions for each curve, the measured data were fitted with a power function, and the data calculated from the fits were averaged within a fixed range of the x-axis. The actual evaluated slope, which slightly differed from the desired slope, also needed to be taken into account. A histogram of the actual slopes is shown in the same figure, where the median value of the slope is used as a representative value on the x-axis, and the average friction/film thickness is plotted on the y-axis. It defines a single point in the final figure highlighted by a red circle. In the case of inclined surfaces, six data points for two slopes (approximately 3 and 12 μm) were fitted by another power function (on the right side of Figure 8b). The final value of friction or film thickness for relative comparison of the overall performance of inclined surfaces was obtained from this fit, averaged over a range of slopes from 2 to 12 μm . The error bars at each data point represent the uncertainty of the mean value obtained as the standard deviation of fit residues divided by the square root of the number of data points in the dataset.

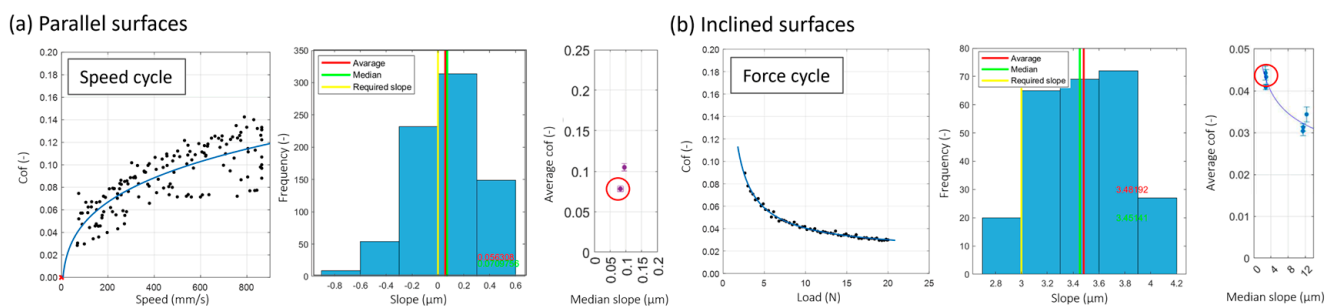


Figure 8. Scheme of average value evaluation in (a) Speed cycle for parallel surfaces and (b) Force cycle for inclined surfaces. The figures in the middle column are histograms of actual slopes evaluated from measured frames. The right figure shows the plot of the final average values. The red circles highlight the obtained single value.

3.1. Parallel Surfaces

The average coefficient of friction and the average central film thickness, depending on the median slope, are presented for parallel surfaces for the Force cycle in Figure 9 and

for the Speed cycle in Figure 10. The Speed cycle includes conditions represented by a hydrodynamic parameter $\eta u/PB$ from 2.6×10^{-6} to 4.6×10^{-5} , while the force cycle ranges from 4.6×10^{-5} to 1.8×10^{-4} . Repetitions in experiments are plotted as individual points, where error bars represent standard uncertainty on the average value, calculated from residues between the fit and the measured data. The median slope on the x-axis means that practical conditions could approach the zero value with some finite accuracy. The standard deviation of the actual slope values evaluated from the fluorescence method is typically a $0.2\text{--}0.3 \mu\text{m}$ surface slope on a 5.25 mm length, i.e., $\pm 0.002\text{--}0.003^\circ$. A slightly positive value of the slope was preferred due to the highly nonlinear responses of the friction to negative slopes (diverging gaps).

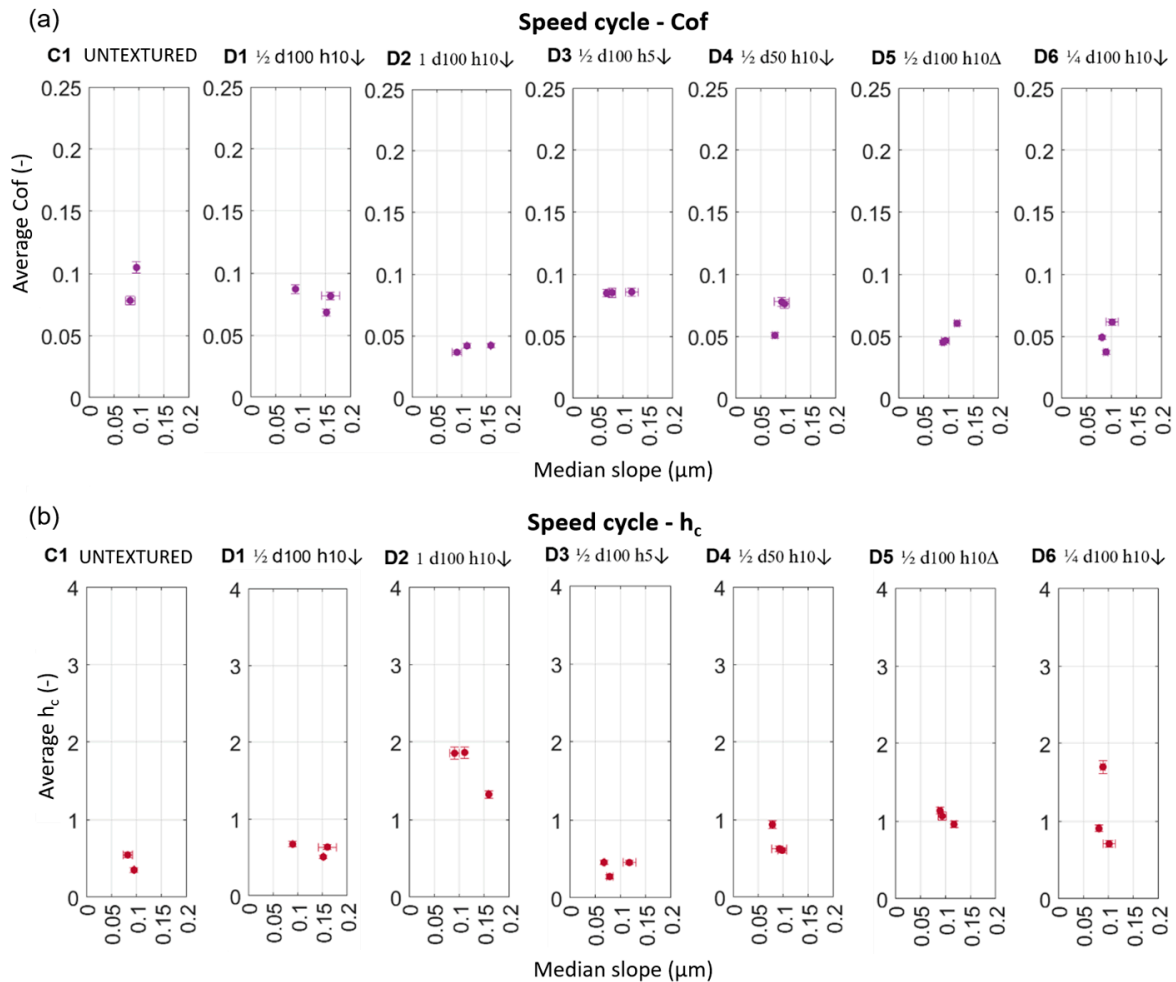


Figure 9. Comparison of all tested samples for (a) the average coefficient of friction and (b) average film thickness in the Force cycle.

From Figures 9 and 10, it is evident that, in general, a lower friction and a higher film thickness provide textured surfaces. The scatter of friction and film thickness results is relatively large, especially in the Force cycle. It resembles the system's sensitivity to inclination, where it is not evident what the trend line of friction and film thickness on the surface slope is. There could be variable contributions from the global wedge action due to global surface inclination, from the pseudo-wedge action due to partial texturing, and from the local hydrodynamic effects of texture, similar to those of isotropic surface roughness. Different textures promote these effects differently, as the parameters of all three effects are dissimilar for individual samples.

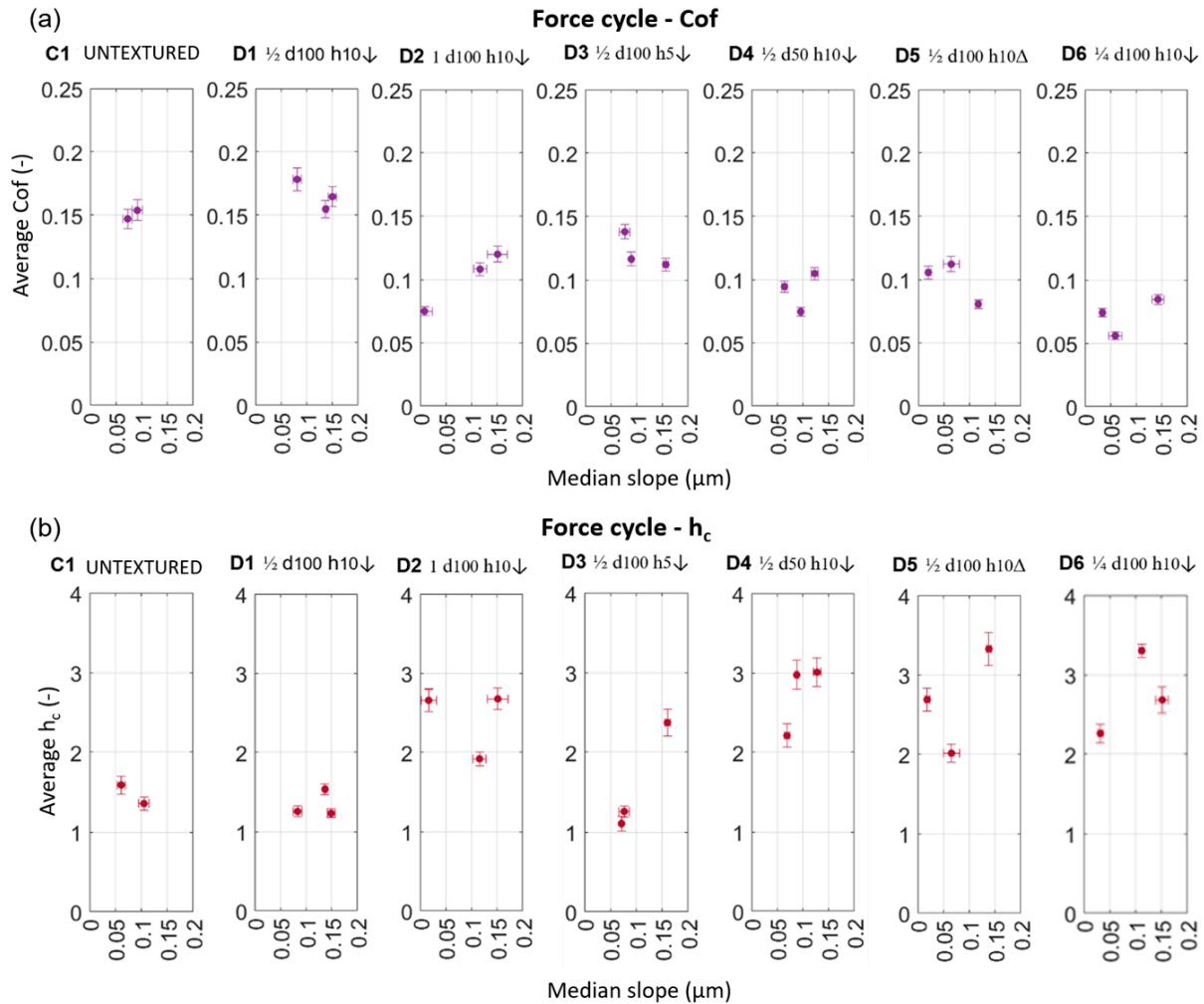


Figure 10. Comparison of all tested samples for (a) the average coefficient of friction and (b) average film thickness in the Speed cycle.

The overall average difference between the results for the smooth sample and the textured samples is shown for parallel surfaces in Figure 11, separately for the Speed and Force cycles. Error bars in the plots represent the cumulative standard uncertainty of the mean value, calculated from the variability of data points in Figures 9 and 10 for the reference case (smooth surface) and textured samples. Most of the samples exhibit an improvement in friction and film thickness (i.e., a decrease in friction and an increase in film thickness), except for the relatively small effects observed in the D1 and D3 textures. Sample D6 demonstrated the most significant positive effect. This sample has texture concentrated at the inlet (see Figure 2) with one-quarter texture coverage. On the other hand, the D2 sample, which has full surface coverage, shows a similar average improvement. As overviewed in [32], several publications have reported that full surface texturing is generally less effective than partial texturing due to the absence of the pseudo-wedge effect. However, numerical simulations [33] have shown that when a texture is properly positioned within a computational domain and using periodic boundary conditions, even the full surface texturing can lead to a positive pressure build-up without cavitation. This observation is consistent with the experimental results presented later in this section. Again, this shows the high sensitivity of the performance to small changes. It is considered that all three effects discussed earlier may play a significant role, and additionally, the specific surface flatness or waviness characteristics are stochastic for each sample.

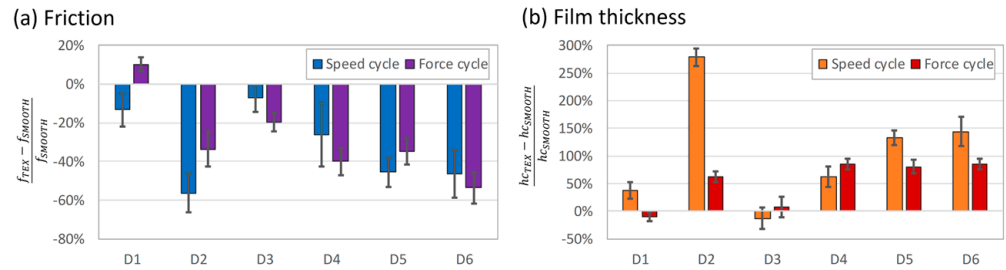


Figure 11. The average difference of (a) friction and (b) film thickness between smooth and textured samples.

Figure 12 provides a closer look at the measured data of samples D1, D2, and D6, specifically for the Force cycle. These samples have the same depth-to-diameter ratio but different coverage areas. The central film thickness, depending on the load, falls more rapidly for the D6 sample compared to the other two, D1 and D2. These two have a similar trend in central film thickness, where the fully covered sample D2 appears to provide a higher film thickness with a constant shift of approximately 1.2 μm. It can be assumed that all three samples represent different hydrodynamic configurations, where texture localization changes the effective pseudo-wedge, various texture coverages promote local surface roughness effects differently, and certain effects can have a stochastic geometry of the samples (limited flatness and waviness). Without detail and systematic numerical simulations, it is difficult to provide clear and solid explanations.

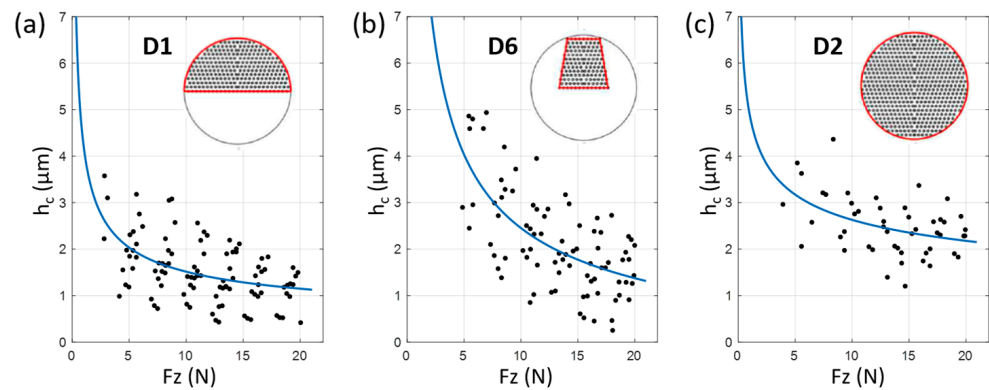


Figure 12. Data of central film thickness depending on normal load for textured sample (a) D1 with 1/2 coverage, (b) D6 with 1/4 coverage, and (c) D2 with full coverage.

The Force cycle gives a higher average film thickness and a higher average coefficient of friction compared to the Speed cycle. It has to be considered that the Force cycle represents a higher hydrodynamic parameter $\frac{\mu U}{PB}$ compared to the Speed cycle. Nevertheless, the question is whether there is any general link between film thickness and friction in situations of parallel surfaces. In Figure 13, the measured and predicted coefficients of friction are plotted based on actual measured film thickness data. The prediction is a simple calculation of frictional losses thanks to the Couette flows, considering a laminar flow in a flat circular area and ambient conditions viscosity, according to:

$$CoF_{teor.} = \frac{\eta u_m S}{h_c F_n}, \tag{1}$$

where u_m is the average speed in cycles, S is the surface area, h_c is the average film thickness, and F_n is the average load in the cycle. There is a relatively good match between predicted and measured values for the Force cycle, while the prediction gives a higher

friction compared to the measurement for the Speed cycle. For both cycles, there is linearity between predicted and measured friction, which means that film thickness corresponds to friction. The reason for the different slope and offset of the linear Speed cycle trend-line may be due to different significant contributors to the friction/lubrication.

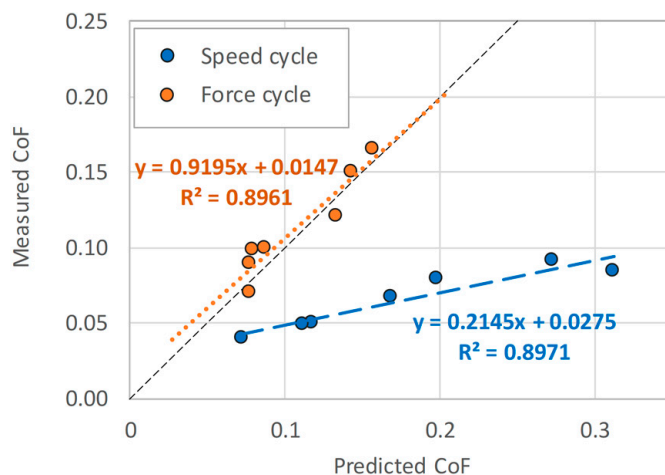


Figure 13. Plot of measured and predicted coefficient of friction based on measured film thickness, separately for the Speed and Force cycles.

Thanks to direct optical observation of the sliding contact, it was possible to observe cavitation phenomena. The cavitation occurred in all textured samples to various extents only under the conditions of parallel surfaces. Figure 14 presents the average filling of individual textures on the surface by a lubricant throughout the entire experimental sequence under parallel surface conditions. Because fluorescence emission is proportional only to the volume of lubricant present, air within the textures does not contribute to the signal. Since all texture dimples possess nominally identical depths, the average intensity at each point was calculated from the complete frame sequence of the test cycle (Figure 1b). The resulting intensity mapping is graded using a six-color scale, where black represents maximum intensity (full lubricant filling) and yellow denotes the minimum. This filling level serves as a direct measure of in-texture cavitation, where color mapping includes both the probability of cavitation of individual pockets and the level of lubricant filling in individual frames. It can be observed that all textured surfaces exhibit some level of cavitation; the lowest level appears to be for the D6, D4, and D2 samples. Experimental observations revealed that the extent of cavitation decreases as the slope of the contact surfaces increases. Cavitation was completely eliminated when the slope exceeded a threshold of approximately $0.35 \mu\text{m}$. Beyond this value, the hydrodynamic pressure generated within the global hydrodynamic wedge was sufficient to suppress the formation of negative pressure.

By comparing the CoF decrease with cavitation localization, it is evident that cavitation in the central region of the contact is associated with no significant improvement in friction, especially when the cavitation spreads over almost the entire contact width. The individual mechanisms and plots of a pressure field and a fractional film content are illustrated in Figure 3 of Ref. [32]. These figures clearly demonstrate the difference in the pressure field between cases when the texture acts globally (pseudo-wedge mode), providing a higher load-carrying capacity compared to the local mode of texture function. In the latter, cavitation limits negative pressure drops, while positive pressure peaks provide net-positive load support. Nevertheless, the current result for the fully textured surface D2 shows a much smaller extent of cavitation. Although this deviates from the situation

depicted in Figure 3e of [32], it is in agreement with the numerical results presented in [33]. This is presumably connected to a significant rise in global pressure at the center of the contact, which ensures that the pressure drop in the diverging part of the texture features does not reach the point of cavitation. Moreover, it can be assumed that contacts with partial cavitation provide a certain space for optimizing load-carrying capacity. It would be connected to a higher film thickness in this case, but not necessarily lower friction due to the fact that cavitated zones contain a mixture of lubricant and air with a lower shear resistance.

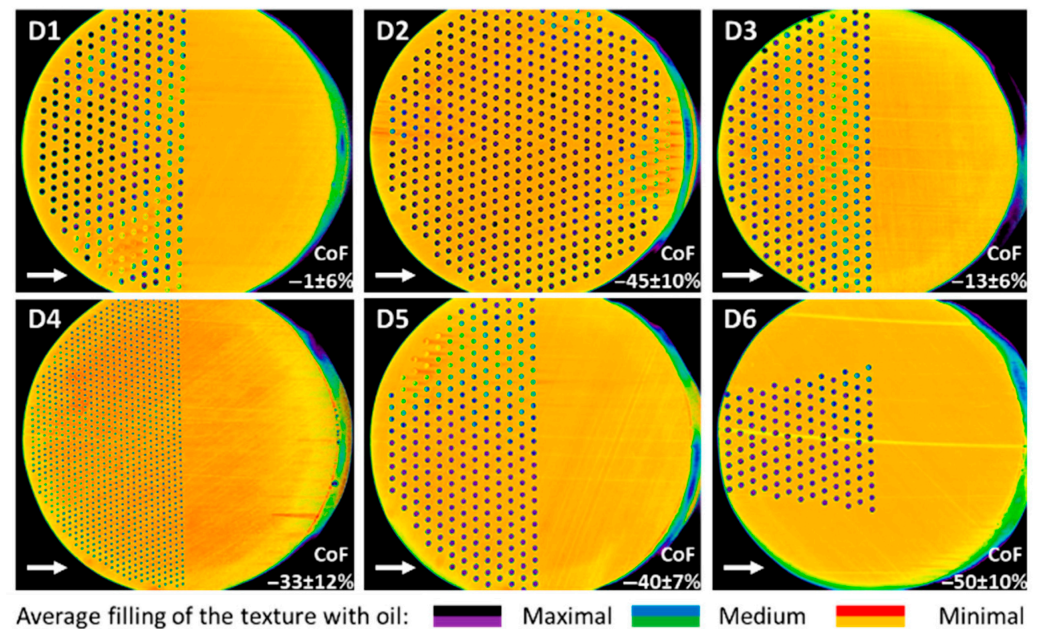


Figure 14. A colormap of average filling of textures by lubricant, i.e., the measure of in-texture cavitation, within the complete experimental cycle at the case of parallel surfaces. The arrows show the direction of the sliding speed.

The fully textured D2 sample achieves a relatively stable and high film thickness value under various loads. This sample could have the highest local effect of texture due to the surface roughness. On the other hand, the sample with partial texturing (D6) achieves a high film thickness at low loads (up to approximately 10 N), but its ability to form a lubricating film decreases with increasing load. The dominance of the sample texture on a quarter of the surface may be attributed to the lateral outflow of lubricant from the contact. Assuming that the hydrodynamic pressure occurs above the textured area, which does not border the edges of the sample, there is not as pronounced a lateral lubricant outflow from the contact.

3.2. Inclined Surfaces

Due to small differences between the results for the smooth and textured samples, as shown in Figure 7, a similar approach to that described in Section 3.1 of data fitting and subsequent averaging was applied to the Speed and Force cycles. In this case, an additional fit was made to the average data depending on the median slope. Results for the Force cycle are shown in Figure 15, and for the Speed cycle in Figure 16. As can be seen in certain cases, the variability of the film thickness data is small compared to the friction data points. Specifically for the inclined surfaces, the absolute friction values are small, typically around 0.2 N. In general, the residuals from the friction data fitting are small. A representative picture of the measured points and the fit is shown in Figure 8b. A larger influence is attributed to the imperfect zeroing of the load cell or the limited independence of the frictional and normal load cells. The latter was tuned in a preparation

sequence before actual measurement, where the pin was pressed from zero to maximum and back to zero load in the normal direction at the static conditions of parallel surfaces. The effect on the frictional force was evaluated, and the angle between the pin holder and the arm that transmits the frictional force was tuned to minimize the dependence. It was possible to achieve independence on the level of 0.25%, i.e., this contributes to friction force uncertainty by 0.05 N for a 20 N load case. Better tuning is not effective since other effects have similar effects. The contact pressure acting normal to the inclined surface has a small force component in the frictional direction, which can be as high as 0.2% for a 12 μm inclination.

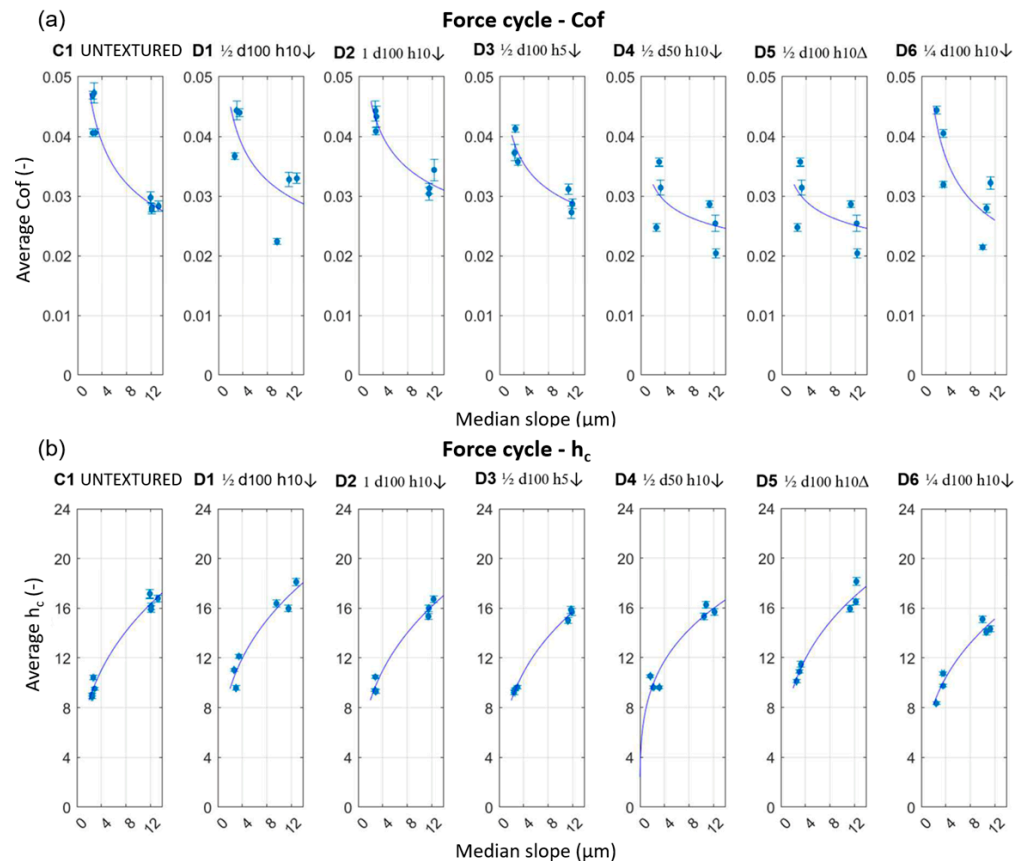


Figure 15. Comparison of all tested samples for the Force cycle and inclined surface; (a) friction coefficient difference and (b) central thickness difference.

The average difference of the film thickness and friction between the textured samples and the smooth sample is presented in Figure 17 for the inclined surfaces. The Speed cycle represents the range of characteristic hydrodynamic parameter $\frac{1}{m^2} \frac{\eta u}{PB}$ from 0.389 to 242. For the Force cycle, it is from 6.73 to 969. The error bars represent the combined uncertainty of the average value, which arises from the variability of results for both the reference, i.e., the smooth surface, and the actual textured surface. The variability is calculated from the residuals between the actual averaged data and the fits in Figures 15 and 16. The majority of textured samples do not exhibit a significant decrease in friction or an increase in film thickness. The largest friction and film thickness improvement is for the D5 sample at the level of 10–25% in friction and 2–5% in film thickness.

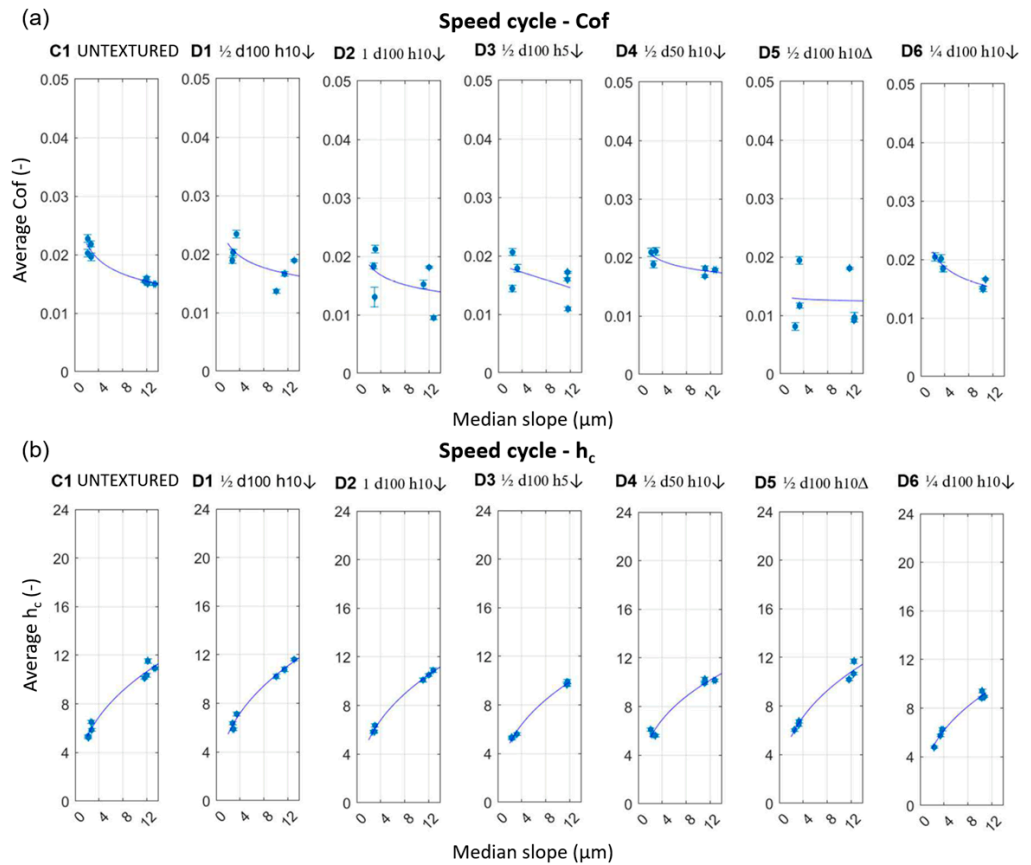


Figure 16. Comparison of all tested samples for the Speed cycle and inclined surface; (a) friction coefficient difference and (b) central thickness difference.

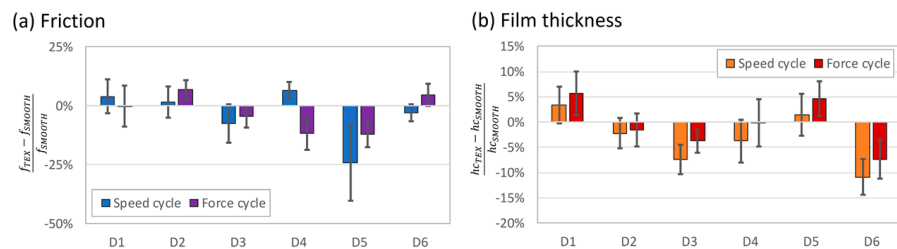


Figure 17. The average difference in (a) friction and (b) central film thickness between the textured samples and the smooth sample.

Overall, the Speed cycle yields a lower average friction difference compared to the Force cycle. Again, the potential phenomena can be considered and discussed. It is the effect of texture on the pseudo-wedge, promoting its global hydrodynamic effect, local hydrodynamic effects from the surface roughness perspective, and the effects of other geometry imperfections of sliding surfaces. A quantitative picture can be built by considering the height scale of surface roughness, surface waviness, and radius of curvature, as included in Table 2. The RMS surface roughness Sq value is around $3.5 \pm 0.35 \mu\text{m}$ for D1, D2, D5, and D6 and around $1.7 \pm 0.25 \mu\text{m}$ for D3 and D4, compared to the smooth sample C1 with the value of $0.07 \mu\text{m}$. Therefore, the roughness height of textured surfaces is comparable to the surface slope in experiments conducted with a $3 \mu\text{m}$ nominal inclination; thus, local hydrodynamic effects can play a significant role. The limited flatness of the samples, expressed as the radius of curvature R_s , ranges from 31.2 to 159.4 m, representing a height difference of 0.02 to 0.11 μm on the pin diameter. The macroscopic surface geometry irregularities were analyzed for parallel surfaces in [34] and for tilting pad thrust bearing

in [35]. The results support that the amplitudes of waviness in the present samples have a negligible effect under conditions of inclined surfaces. The RMS value of surface waviness Wq is between 0.026 and 0.144 μm , which is much smaller compared to the inclination wedge discussed in this section.

Comparing the relative differences between textured and smooth surfaces, it is evident that textures contribute less to hydrodynamic lubrication on inclined surfaces than on parallel ones. A primary function of texturing is its ability to alter global hydrodynamic conditions within the contact area. Partially texturing the inlet region creates a variable average cross-sectional area in the hydrodynamic gap, even when surfaces are parallel. This configuration can generate a macroscopic pressure field analogous to a Rayleigh step geometry, allowing textures to produce an effective hydrodynamic wedge (the pseudo-wedge). Essentially, the texture features shift the surface's mean plane for a specific portion of the contact.

The impact of the current texture parameters is quantified by the Height shift values (H_s), primarily determined by coverage and depth. Data evaluated from the 3D optical profilometry of the real samples are in Table 2. The values range from 0.658 to 1.82 μm for the textured surfaces. The H_s parameter represents the maximum potential effect on the pseudo-wedge, assuming no cavitation and laminar flow within the textures. These values are insignificant compared to the tested and practical inclination slopes. Dobrica and Fillon [33] analyzed in detail the conditions under which Reynolds' approach, with the laminar flow assumption, is valid. For current hydrodynamic conditions and textures with aspect ratio $d/h \geq 10$ the error in load-carrying capacity is less than 5%.

Since the maximum load-carrying capacity of a hydrodynamic wedge occurs when the surface slope is comparable to the minimum film thickness, it is more effective to adjust the global surface slope in applications where inclination is physically possible. However, in parallel surface configurations where inclination is impossible, texturing becomes the primary mechanism for enhancing load-carrying capacity and friction through global or local hydrodynamic effects.

Although the operational conditions covered a wide range of hydrodynamic lubrication, expressed by the dimensionless parameter $\frac{1}{m^2} \frac{\eta u}{PB}$, ranges from 0.389 to 969, the final relative comparison was averaged across two broad sections of this range. Consequently, there may be specific subdomains where the effect of texture is more pronounced than the averages suggest. Nevertheless, it is clear that surface textures have a significant impact under parallel surface conditions. This study represents one of the first experimental investigations to focus on the simultaneous measurement of film thickness and friction for parallel surfaces. Three distinct contributions of the textures were discussed: a global hydrodynamic effect (pseudo-wedge), a local hydrodynamic effect, and the influence of surface non-flatness (waviness). Further experimental and numerical work is required to clarify the relative importance of these practical aspects on realistic surfaces within nominally parallel gaps.

4. Conclusions

This study investigated the effects of surface texturing on hydrodynamic lubrication using simultaneous measurements of friction and film thickness by a light-induced fluorescence method. The proposed methodology enables precise experimental analysis of inclined and parallel surfaces with the measurement of the real wedge slope. Based on the comparison of smooth and textured steel surfaces under parallel and inclined configurations, the following conclusions are drawn:

- Surface texturing significantly enhances tribological performance in nominally parallel gaps. Textures generate a hydrodynamic pseudo-wedge, leading to lower friction and higher film thickness compared to smooth surfaces. The most substantial im-

provement was observed with partial texturing concentrated at the inlet (quarter coverage), which outperformed full coverage patterns.

- In contacts with a physical wedge (inclinations of 3–12 μm), the effect of texturing is small. The geometric inclination dominates pressure generation, showing that the influence of textures has a marginal influence compared to the smooth reference.
- In-texture cavitation was observed for parallel configurations, where the cavitation localization in the contact center was connected to the smallest friction improvement. Cavitation was suppressed and eventually eliminated when the surface inclination exceeded a threshold of approximately 0.35 μm .
- The positive hydrodynamic effect observed in fully textured samples implies that surface texture induces a local hydrodynamic response, behaving similarly to surface roughness.

In future studies, the ring-on-disk approach has the potential to provide a stable alignment closer to ideal parallel surfaces. Furthermore, experiments utilizing sapphire disks will enable a more detailed examination of the transition from mixed to full-film lubrication.

Author Contributions: Conceptualization, M.O. and P.Š.; methodology, P.Š. and J.K.; validation, M.H.; investigation, P.Š., M.O., and J.K.; writing—original draft preparation, P.Š. and J.K.; writing—review and editing, M.O. and M.H.; supervision, I.K.; project administration, P.P.; funding acquisition, M.H. All authors have read and agreed to the published version of the manuscript.

Funding: This research was supported by the Czech Science Foundation (Project No. 22-29874S) and the MEBioSys—‘Mechanical Engineering of Biological and Bio-inspired Systems’ project funded as no. CZ.02.01.01/00/22_008/0004634 by Programme Johannes Amos Comenius, call Excellent Research.

Data Availability Statement: Experimental data, processed datasets, generated and analyzed in this study are openly available in Zenodo under the DOI: <https://doi.org/10.5281/zenodo.17860487>. The manuscript preprint is available in the Zenodo repository under DOI: <https://doi.org/10.5281/zenodo.18063500>.

Conflicts of Interest: The authors declare no conflicts of interest.

Abbreviations and Nomenclature

B	length of slider (m)
CoF	coefficient of friction (-)
F	slider load (N)
F_n	average slider load in test cycle (N)
h_1	entrance (inlet) film thickness (μm)
h_c	central film thickness (μm)
H_s	height shift of textured surface mean plane (μm)
h_m	minimum (exit) film thickness (μm)
m	relative slope of the slider (-)
L	width of the slider (m)
LIF	Light-induced fluorescence
P	mean contact pressure, F/LB (Pa)
R_s	slider surface nonflatness expressed as radius of curvature (m)
S	nominal contact area of the pin (m^2)
S_q	RMS value of surface roughness height (μm)
t	temperature ($^{\circ}\text{C}$)
u	sliding speed (m/s)
u_m	average sliding speed in test cycle (m/s)
W_q	RMS value of surface waviness height (μm)
δ	surface slope (μm)

References

1. Gropper, D.; Wang, L.; Terry, J.H. Hydrodynamic lubrication of textured surfaces: A review of modeling techniques and key findings. *Tribol. Int.* **2015**, *94*, 509–529. [[CrossRef](#)]
2. Gachot, C.; Rosenkranz, A.; Hsu, S.M.; Costa, H.L. A critical assessment of surface texturing for friction and wear improvement. *Wear* **2017**, *372–373*, 21–41. [[CrossRef](#)]
3. Wang, Z.; Ye, R.; Xiang, J. The performance of textured surface in friction reducing: A review. *Tribol. Int.* **2022**, *177*, 108010. [[CrossRef](#)]
4. Brizmer, V.; Kligerman, Y.; Etsion, I. A Laser Surface Textured Parallel Thrust Bearing. *Tribol. Int.* **2003**, *46*, 397–403. [[CrossRef](#)]
5. Tala-Ighil, N.; Fillon, M.; Maspeyrot, P. Effect of textured area on the performances of a hydrodynamic journal bearing. *Tribol. Int.* **2011**, *44*, 211–219. [[CrossRef](#)]
6. Codrignani, A.; Frohnapfel, B.; Magagnato, F.; Schreiber, P.; Schneider, J.; Gumbsch, P. Numerical and experimental investigation of texture shape and position in the macroscopic contact. *Tribol. Int.* **2018**, *122*, 46–57. [[CrossRef](#)]
7. Cupillard, S.; Cervantes, M.J.; Glavatskih, S. Pressure Buildup Mechanism in a Textured Inlet of a Hydrodynamic Contact. *J. Tribol.* **2008**, *130*, 021701. [[CrossRef](#)]
8. Manser, B.; Belaidi, I.; Hamrani, A.; Khelladi, S.; Bakir, F. Texture shape effects on hydrodynamic journal bearing performances using mass-conserving numerical approach. *Tribol. Mater. Surf. Interfaces* **2019**, *14*, 33–50. [[CrossRef](#)]
9. Hsu, S.M.; Jing, Y.; Hua, D.Y.; Zhang, H. Friction reduction using discrete surface textures: Principle and design. *J. Phys. D Appl. Phys.* **2014**, *47*, 335307. [[CrossRef](#)]
10. Bai, L.; Meng, Y.; Zhang, V. Experimental Study on Transient Behavior of Cavitation Phenomenon in Textured Thrust Bearings. *Tribol. Lett.* **2016**, *63*, 27. [[CrossRef](#)]
11. Cross, A.T.; Sadeghi, F.; Cao, L.; Rateick, R.G.; Rowan, S. Flow Visualization in a Pocketed Thrust Washer. *Tribol. Trans.* **2012**, *55*, 571–581. [[CrossRef](#)]
12. Zhang, J.; Meng, Y. Direct Observation of Cavitation Phenomenon and Hydrodynamic Lubrication Analysis of Textured Surfaces. *Tribol. Lett.* **2012**, *46*, 147–158. [[CrossRef](#)]
13. Vlădescu, S.C.; Ciniero, A.; Tufail, K.; Gangopadhyay, A.; Reddyhoff, T. Looking into a laser textured piston ring-liner contact. *Tribol. Int.* **2017**, *115*, 140–153. [[CrossRef](#)]
14. Obert, P.; Füsser, H.J.; Bartel, D. Oil distribution and oil film thickness within the piston ring-liner contact measured by laser-induced fluorescence in a reciprocating model test under starved lubrication conditions. *Tribol. Int.* **2018**, *129*, 191–201. [[CrossRef](#)]
15. Liang, X.; Yan, X.; Ouyang, W.; Wood, R.J.K.; Kuang, F.; Liu, Z.; Zhou, X. Comparison of measured and calculated water film thickness of a water-lubricated elastically supported tilting pad thrust bearing. *Surf. Topogr. Metrol. Prop.* **2019**, *7*, 045010. [[CrossRef](#)]
16. Myant, C.; Reddyhoff, T.; Spikes, H.A. Laser-induced fluorescence for film thickness mapping in pure sliding lubricated, compliant, contacts. *Tribol. Int.* **2010**, *43*, 1960–1969. [[CrossRef](#)]
17. Rosenkranz, A.; Costa, H.L.; Profito, F.J.; Gachot, C.; Medina, S.; Dini, D. Influence of surface texturing on hydrodynamic friction in plane converging bearings—An experimental and numerical approach. *Tribol. Int.* **2019**, *134*, 190–204. [[CrossRef](#)]
18. Bulut, D.; Bader, N.; Poll, G. Cavitation and film formation in hydrodynamically lubricated parallel sliders. *Tribol. Int.* **2021**, *162*, 107113. [[CrossRef](#)]
19. Cheong, J.; Wigger, S.; Füsser, H.J.; Kaiser, S.A. The oil film around a cylindrical micropore in a sliding contact visualized by fluorescence microscopy on a tribometer. *Tribol. Int.* **2021**, *165*, 107309. [[CrossRef](#)]
20. Song, H.; Mu, H.; Zhu, D.; Zheng, Q.; Kuang, F. Laser-Induced Fluorescence (LIF) Method-Based Research on the Influence of Textured Water-Lubricated UHMWPE Bearing Tribological Performance. *Tribol. Lett.* **2025**, *73*, 4. [[CrossRef](#)]
21. Guo, F.; Wong, P.L.; Fu, Z.; Ma, C. Interferometry Measurement of Lubricating Films in Slider-On-Disc Contacts. *Tribol. Lett.* **2010**, *39*, 71–79. [[CrossRef](#)]
22. Li, X.; Guo, F.; Yang, S.; Wong, P.L. Measurement of Load-Carrying Capacity of Thin Lubricating Films. *J. Tribol.* **2012**, *134*, 044501. [[CrossRef](#)]
23. Liu, H.; Guo, F.; Guo, L.; Wong, P.L. A Dichromatic Interference Intensity Modulation Approach to Measurement of Lubricating Film Thickness. *Tribol. Lett.* **2015**, *58*, 15. [[CrossRef](#)]
24. Guo, L.; Wong, P.L.; Gachot, C. Facilitating the Study of the Texturing Effect on Hydrodynamic Lubrication. *Lubricants* **2018**, *6*, 18. [[CrossRef](#)]
25. Jing, Z.; Guo, F.; Jin, W.; Kalin, M.; Polajnar, M. Study on the influence of interfacial slip on the lubrication performance of a step slider bearing. *Tribol. Int.* **2022**, *176*, 107822. [[CrossRef](#)]
26. Cherdantsev, A.; Бобылев, A.B.; Guzanov, V.V.; Kvon, A.Z.; Kharlamov, S.M. Measuring liquid film thickness based on the brightness level of the fluorescence: Methodical overview. *Int. J. Multiph. Flow* **2023**, *168*, 104570. [[CrossRef](#)]
27. Chen, H.; Wang, W.; Ge, X.; Liang, H. Pixel-dependent laser-induced fluorescence method for determining thin liquid film thickness distribution. *Phys. Fluids* **2024**, *36*, 012111. [[CrossRef](#)]

28. Pusterhofer, M.; Maier, M.R.; Scharf, R.; Haumer, F.; Grün, F. Hydrodynamic performance testing of artificial textures using a novel pin-on-disc test method. *Front. Mech. Eng.* **2025**, *11*, 1473028. [[CrossRef](#)]
29. Beamish, S.; Li, X.; Brunskill, H.; Hunter, A.; Dwyer-Joyce, R.S. Circumferential film thickness measurement in journal bearings via the ultrasonic technique. *Tribol. Int.* **2020**, *148*, 106295. [[CrossRef](#)]
30. *ISO 25178-2:2021; Geometrical Product Specifications (GPS) - Surface Texture : Areal. Terms, Definitions and Surface Texture Parameters.* International Organization for Standardization: Geneva, Switzerland, 2021.
31. Raimondi, A.A.; Boyd, J. Applying Bearing Theory to the Analysis and Design of Pad-Type Bearings. *Trans. Am. Soc. Mech. Eng.* **1955**, *77*, 287–309. [[CrossRef](#)]
32. Marian, M.; Almqvist, A.; Rosenkranz, A.; Fillon, M. Numerical micro-texture optimization for lubricated contacts—A critical discussion. *Friction* **2022**, *10*, 1772–1809. [[CrossRef](#)]
33. Dobrica, M.B.; Fillon, M. About the validity of Reynolds equation and inertia effects in textured sliders of infinite width. *Proc. Inst. Mech. Eng. Part J J. Eng. Tribol.* **2008**, *223*, 69–78. [[CrossRef](#)]
34. Charitopoulos, A.; Fillon, M.; Papadopoulos Ch, I. Numerical investigation of parallel and quasi-parallel slider bearings operating under ThermoElastoHydroDynamic (TEHD) regime. *Tribol. Int.* **2018**, *149*, 105517. [[CrossRef](#)]
35. Zoupas, L.; Wodtke, M.; Papadopoulos Ch, I.; Wasilczuk, M. Effect of manufacturing errors of the pad sliding surface on the performance of the hydrodynamic thrust bearing. *Tribol. Int.* **2019**, *134*, 211–220. [[CrossRef](#)]

Disclaimer/Publisher’s Note: The statements, opinions and data contained in all publications are solely those of the individual author(s) and contributor(s) and not of MDPI and/or the editor(s). MDPI and/or the editor(s) disclaim responsibility for any injury to people or property resulting from any ideas, methods, instructions or products referred to in the content.